

Boundary driven shear layer instabilities in a rotating fluid

Nathanaël Schaeffer

LGIT, Université Joseph Fourier, Grenoble, France^{*}

Philippe Cardin

LGIT, Université Joseph Fourier and CNRS, Grenoble, France

(Dated: May 22, 2019)

We study the destabilization of a shear layer, produced by differential rotation of a rotating axisymmetric container. For small forcing, this produces a shear layer, which has been studied by Stewartson and is almost invariant along the rotation axis direction. When the forcing increases, instabilities develop. The way these instabilities grow depends strongly on the geometry of the container. If the depth is constant, the instability develops without breaking the Proudman-Taylor constraint. However, when the depth is not constant (in a spherical shell for instance), the instability has to break the Proudman-Taylor constraint, and thus, the threshold is higher. We develop a quasi-geostrophic two-dimensional model, whose main original feature is to handle the mass conservation correctly, resulting in a divergent two-dimensional flow, and valid for any finite slope. We use it to investigate scalings and asymptotic laws by a simple linear theory and we find an asymmetry between positive and negative differential rotation; we also propose a correction to take the ageostrophy of the shear layer into account. Implemented in a numerical code, it allows us to span a broad range of parameter to study the threshold. We also present some experimental results, validating our model and showing its limits.

I. INTRODUCTION

The spherical Taylor-Couette problem, where two spheres are rotating at different speeds, will be the base of our forthcoming sodium experiment, which is under construction, and which goal is to understand the magnetostrophic equilibrium [5]. This type of flow has been widely studied [see e.g. 1, 16, 26]. However, the range of parameter that interests us, that is a strong global corotation with a small differential rotation, has never been studied as far as we know.

The linear problem resulting in cylindrical shear layers aligned with the axis of rotation has been studied by [23] in the inviscid case. He pointed out the nested shear layer structure and their scaling. This problem is closely related to the simpler case of a split cylinder solved earlier by [22] too. In that case, the structure of the shear layer is simpler, but there is still a nested structure. The general structure of these detached shear layers is studied by [15], by focusing on the singularities of the boundary-layer equations. Later, a numerical study has been done by [7], recovering the features and scalings predicted by Stewartson.

The linear stability of this kind of layers has been theoretically investigated by [3] who applied the regular stability theory to the pressure equation in both cases of constant and varying depth, recovering some kind of Rayleigh criterion. However, the existing experimental studies are not in quantitative agreement with these results.

The setup of [11], with a horizontal disk rotating differentially in a flat cylindrical tank, gives rather strange results and unexpected power-laws. They also observed a strong asymmetry between positive and negative differential rotation. Later, [17] perform a similar experiment but with the differential rotation concentrated on the bottom of their flat tank. They find a critical local Reynolds number for the destabilization of the flow. Their linear theory which includes Ekman friction and internal viscosity is in good quantitative agreement with their results. They point out that the internal viscosity is very important to reproduce accurately the experimental results. More recently, [9] reproduced almost exactly the case studied by [22]. They found that the instability is a supercritical Hopf bifurcation and that the behaviour of the flow does not depend strongly on the sign of the differential rotation. The threshold of instability is governed by a critical local Reynolds number, but the theory of Niino & Misawa predicts a value much higher than the observed one. [14] investigated the shear-flow instabilities with a parabolic tank and a free surface. They studied both cases with constant depth or varying depth and pointed out that the varying depth has a stabilizing effect, as predicted by the linear theory. However, their setup could not investigate the rotation rate dependence.

^{*}Nathanael.Schaeffer@ujf-grenoble.fr

Furthermore, the destabilization of a shear layer in a rotating system is of general geophysical interest. Shear layer dominated by the Coriolis force, are found in natural systems, as in the atmosphere or in the ocean, as well as on other planets like the jets of Jupiter, which might be unstable and responsible for the observed big eddies. The variation of the Coriolis force with latitude, known as beta-effect, can be modelled in laboratory experiments by using a varying depth rotating container [see e.g. 19].

The further organization of this paper is as follows. In §II, we derive the equations of our model, that will be used to address the problem in the next sections, through numeric calculation and theoretical analysis of the equations. §III presents results concerning the Stewartson layer, §IV focuses on the stability threshold of this shear layer in the asymptotic regime and how it compares with various experiments. §V gives corrections for the threshold at finite Ekman numbers that explain both numerical and experimental results, while §VI addresses the spatial structure of this instability near the threshold. Finally §VII contains a summary and discussion.

II. QUASI-GEOSTROPHIC MODEL

The two-dimensional quasi-geostrophic (QG) model we present here has been developed to study the flow in rapidly rotating container, invariant by rotation around the rotation axis. We use the cylindrical coordinate system $(\mathbf{e}_r, \mathbf{e}_\phi, \mathbf{e}_z)$, with r the distance to the axis, ϕ the angle in the plane perpendicular to that axis, and z the height. The container is defined by two functions $z = L_+(r)$ and $z = L_-(r)$, for the top and the bottom surfaces respectively. Here, we first restrict to the simpler case where $L(r) = L_+(r) = -L_-(r)$.

In a frame rotating at angular velocity Ω_0 around the vertical axis z , the flow is described by the Navier-Stokes equation for an incompressible fluid with constant density, including the Coriolis force :

$$\frac{\partial \mathbf{u}}{\partial t} + (\mathbf{u} \cdot \nabla) \mathbf{u} + 2\Omega_0 \wedge \mathbf{u} = -\nabla \Pi + \nu \nabla^2 \mathbf{u} \quad (1)$$

where \mathbf{u} is the fluid velocity field, ν the kinematic viscosity, and Π the pressure field, including centrifugal and gravity forces. We introduce a velocity scale U , a time scale Ω_0^{-1} and as typical length scale R the radial size of the container. We then rewrite equation 1 with non-dimensional quantities :

$$\frac{\partial \mathbf{u}}{\partial t} + Ro (\mathbf{u} \cdot \nabla) \mathbf{u} + 2\mathbf{e}_z \wedge \mathbf{u} = -\nabla \Pi + E \nabla^2 \mathbf{u} \quad (2)$$

with $Ro \equiv U/R\Omega_0$ the Rossby number, $E \equiv \nu/R^2\Omega_0$ the Ekman number, and \mathbf{e}_z the unit vector along the rotation axis.

In our study, we take for typical velocity the one based on the differential rotation $U = R\Delta\Omega$ which is supposed to dominate. Hence, the Rossby number reduces to $\Delta\Omega/\Omega_0$.

A. Proudman-Taylor theorem and z -averaging

For vanishing Ekman and Rossby number, we recover the Proudman-Taylor theorem for a stationary flow : taking the curl of equation 2, we find that

$$\frac{\partial \mathbf{u}}{\partial z} = 0$$

This suggests that for small Rossby and Ekman numbers, the z -variations should be weak and we expect the flow to be mainly two-dimensional for long-period motions ($\gg \Omega_0^{-1}$).

We define the z -averaging by

$$\langle u \rangle = \frac{1}{2L} \int_{-L}^{+L} u(r, z) dz \quad (3)$$

Keeping in mind that L depends on r , we have

$$\frac{\partial \langle u \rangle}{\partial r} = \left\langle \frac{\partial u}{\partial r} \right\rangle + \frac{1}{L} \frac{\partial L}{\partial r} \left(\frac{u(r, +L) + u(r, -L)}{2} - \langle u(r, z) \rangle \right)$$

As a matter of fact, a sufficient condition for the r -derivative to commute with z -averaging is that u is independent of z , that is $u = \langle u \rangle$.

B. Vorticity equation

We now average the z -component of the curl of equation 2 with the additional constraint that u_r and u_ϕ are independent of z (so that we can permute r -derivation and z -averaging). The z -component of the vorticity ω is denoted by ω and is also z -invariant. We obtain

$$\frac{\partial \omega}{\partial t} + Ro \left(u_r \frac{\partial \omega}{\partial r} + \frac{u_\phi}{r} \frac{\partial \omega}{\partial \phi} \right) - (2 + Ro \omega) \left\langle \frac{\partial u_z}{\partial z} \right\rangle = E \nabla^2 \omega \quad (4)$$

Note that we keep the vortex stretching term $\left\langle \frac{\partial u_z}{\partial z} \right\rangle$. All other terms vanish, without any condition on u_z .

C. Mass conservation

The local mass conservation equation

$$\frac{1}{r} \frac{\partial r u_r}{\partial r} + \frac{1}{r} \frac{\partial u_\phi}{\partial \phi} + \frac{\partial u_z}{\partial z} = 0 \quad (5)$$

implies that $\frac{\partial u_z}{\partial z}$ is independent of z , so that we can now draw a global picture of the flow in the frame of our QG-model.

- u_r and u_ϕ are z -invariant
- u_z depends linearly on z .

D. Boundary conditions

At first order, the viscous effects are neglected for the geostrophic flow [see 10], so that we only need to match the free-slip boundary condition $\mathbf{u} \cdot \mathbf{n} = 0$, with \mathbf{n} the *outward* unit vector normal to the surface. Since $\mathbf{n} = \nabla(z \mp L(r))$ at $z = \pm L$, we have

$$u_z \mp u_r \frac{\partial L}{\partial r} \Big|_{z=L} = 0$$

which fully determines u_z . Defining β

$$\beta \equiv \frac{1}{L} \frac{\partial L}{\partial r} \Big|_{z=L} \quad (6)$$

we have

$$u_z = z \beta u_r \quad \frac{\partial u_z}{\partial z} = \beta u_r \quad (7)$$

$\frac{\partial u_z}{\partial z}$ is the vortex stretching term that appears in the vorticity equation 4. It has the same form as the so-called beta-effect, where the Coriolis parameter is varying with latitude, as in the atmosphere [see 19].

E. Ekman pumping

For the particular case $\beta = 0$, corresponding to constant-depth container, the next order approximation is needed in order to model $\left\langle \frac{\partial u_z}{\partial z} \right\rangle$. The next order flow \mathbf{u}^1 is the Ekman pumping flow, which is needed to satisfy no-slip boundary conditions. This pumping flow acts as viscous surface friction on geostrophic cylinder, and is given by [10] :

$$\mathbf{u}^1 \cdot \mathbf{n} \Big|_{\pm L} = \frac{1}{2} E^{1/2} \mathbf{n} \cdot \nabla \wedge \left(\frac{\mathbf{n} \wedge (\mathbf{u} - \mathbf{U}_b) \mp (\mathbf{u} - \mathbf{U}_b)}{\sqrt{|\mathbf{n} \cdot \mathbf{e}_z|}} \right) \quad (8)$$

where \mathbf{U}_b is the velocity of the boundary.

Note that these Ekman layers will not be resolved in our model, but rather parametrized using their asymptotical expression. This can be done because their thickness is supposed to be small ($\delta(\nu/\Omega)^{1/2} \ll R$).

In the case of a constant-depth container 8 reduces to

$$\frac{\partial u_z}{\partial z} = -\frac{E^{1/2}}{2L} (\omega - \Omega_b) \quad (9)$$

where Ω_b is the vorticity associated with the velocity of the boundary U_b . In the general case, 8 leads to an expression of the form

$$\frac{\partial u_z}{\partial z} = E^{1/2} \cdot P(u_r, u_\phi, r) + \beta u_r \quad (10)$$

where P is a function depending of the geometry of the container, linear with respect to the jump of u_r and u_ϕ at the boundary and to their first order derivatives. See Appendix A for the explicit expression for a spherical container.

We have now two distinct cases. The first one is the flat container, where $\beta = 0$. We need to use the Ekman pumping to fully determine the flow. In the other case, with a finite slope, the Ekman pumping flow is asymptotically negligible compared to the slope-induced flow, for small enough Ekman numbers. However, even if small, the Ekman pumping is a dissipative process, whereas the β -term is not. Thus, above the threshold, the Ekman suction may play an important damping role.

In both cases, we reduced the problem to the determination of two components of the velocity, u_r and u_ϕ , depending only on r and ϕ .

F. Scalar function

We introduce a scalar field ψ , defined by

$$u_r \equiv \frac{1}{r} \frac{\partial \psi}{\partial \phi} \quad (11)$$

u_ϕ is now constrained by the three-dimensional mass conservation equation 5, so that for *non-axisymmetric* flows,

$$u_\phi \equiv -\frac{\partial \psi}{\partial r} - \beta \psi \quad (12)$$

$$\omega \equiv -\nabla^2 \psi - \beta \left(\frac{\partial \psi}{\partial r} + \frac{\psi}{r} \right) - \frac{d\beta}{dr} \psi \quad (13)$$

With these equations, we can see that the additional β -terms are negligible for $\beta \lambda \ll 1$, where λ is a typical length scale of the velocity field variations. It reduces then to the widely used small slope approximation [see e.g. 2, 4, 13].

It will be shown later, that at the stability threshold, the typical length scale is of order $E^{1/4}$, so that asymptotically this approximation may be valid at the threshold. However, increasing the forcing, large scale structures will eventually appear, with up to order-one scales, so that we cannot neglect this effect anymore.

Similar approaches have been developed recently. [13] proposed a formulation for ocean modelling but with a regular stream function implying that the mass is not conserved. [25] include the effect of weak topography and Ekman suction. The advantage of their formulation is that the Ekman suction is also considered as a source of horizontal divergence. However the simple expression they used for the Ekman boundary condition implicitly assumes small β , that is nearly flat topography.

G. Axi-symmetric flow

For the axi-symmetric flow, the scalar function formalism does not apply. It is simpler to work with the velocity field rather than with the vorticity. We project the Navier-Stokes equation 2 on \mathbf{e}_ϕ , noting that $(\mathbf{e}_z \wedge \mathbf{u}) \cdot \mathbf{e}_\phi = u_r$ and remembering $\frac{\partial u_\phi}{\partial z} = 0$. Averaging over ϕ to keep only the axi-symmetric component, we obtain

$$\frac{\partial \bar{u}_\phi}{\partial t} + Ro \left(u_r \frac{\partial \bar{u}_\phi}{\partial r} + \frac{\bar{u}_\phi \bar{u}_r}{r} \right) + 2\bar{u}_r = E \left(\nabla^2 \bar{u}_\phi - \frac{\bar{u}_\phi}{r^2} \right) \quad (14)$$

where \bar{u} stands for the ϕ -average of u .

The mass conservation equation reduces to

$$\frac{1}{r} \frac{\partial r \bar{u}_r}{\partial r} + \frac{\partial \bar{u}_z}{\partial z} = 0$$

and using equation 10, we can show that \bar{u}_r is only due to the Ekman pumping and is directly related to \bar{u}_ϕ so that the axi-symmetric part is actually one-dimensional : $\bar{u} = \bar{u}_\phi(r) \mathbf{e}_\phi + O(E^{1/2})$. However, non-linear interactions of non-axi-symmetric modes can produce axisymmetric flow, so that we keep the terms involving \bar{u}_r . Furthermore, the Ekman pumping flow \bar{u}_r^1 , of order $E^{1/2}$ cannot be neglected. Equation 8 reduces to

$$\bar{u}_r^1 = E^{1/2} \frac{\alpha}{2L} (\bar{u}_\phi - U_b) \quad (15)$$

whith

$$\alpha \equiv \left(1 + \left(\frac{dL}{dr} \right)^2 \right)^{1/4} \quad (16)$$

H. Numerical implementation

We wrote a numerical code, that solves the equation of the model described above using the pseudo-stream function formulation. We use a finite difference scheme in the radial direction, and a spectral decomposition in azimuth :

$$\Psi(r, \phi) = \Re \left(\sum_{m \geq 1} \psi^m(r) e^{-im\phi} \right) \quad (17)$$

where $\Re(\psi)$ is the real part of ψ . The time integration is done using the semi-implicit Crank Nicolson scheme for the linear part, and a simple Adams-Bashford scheme for the non-linear terms, which are computed in direct space, as in [2].

1. Outer boundary condition

At the outer boundary, we always have the non-penetration condition $u_r = 0$, so that $\Psi(r = 1) = 0$.

To be consistent, we have to use the same boundary conditions that the one used to model the term $\langle \frac{\partial u_z}{\partial z} \rangle$, that is no-slip for the axisymmetric part

$$\bar{u}(r) = 0$$

For the non-axisymmetric part, we also include the Ekman suction in our model, so that the right boundary condition is $\mathbf{u} = 0$ or

$$\left. \frac{\partial \Psi}{\partial r} \right|_{r=1} = 0 \quad (18)$$

However, when neglecting the Ekman pumping flow, the right boundary condition is *free-slip*, which state that the constraint is vanishing at the outer boundary. This is expressed as $\sigma \cdot \mathbf{e}_r = 0$, with σ the constraint tensor. It reduces to

$$\frac{\partial u_\phi}{\partial r} = \frac{u_\phi}{r}$$

and using the fact that $u_r = 0$ at this boundary,

$$\omega|_{r=1} = -\frac{2}{r} \frac{\partial \Psi}{\partial r} \quad (19)$$

This last boundary condition is used only for comparison purposes.

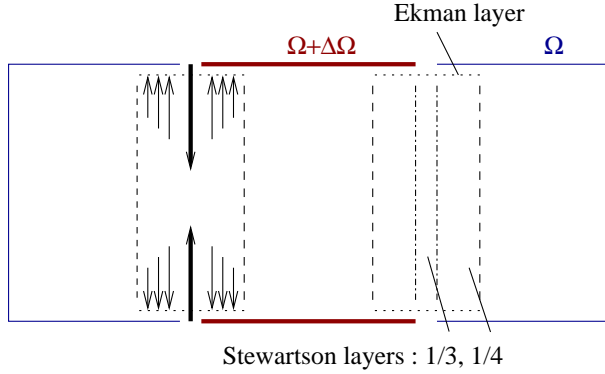


FIG. 1: Sketch of the nested Stewartson layers.

2. Inner boundary condition

At the inner boundary ($r = 0$) u_r and u_ϕ must remain finite, so that

$$\Psi(r = 0) = 0$$

In addition, we are using a polar coordinate system, for which there is a geometrical constraint for a *vector field* \mathbf{u} , at $r = 0$ and $m \neq 1$, we have $u_r^m = 0$ and $u_\phi^m = 0$. This implies that

$$\left. \frac{\partial \psi^m}{\partial r} \right|_{r=0} = 0 \quad , m \geq 2$$

For a *scalar field* ω , there is a analogous condition : for $m \neq 0$, we have $\omega^m = 0$, which implies

$$\left. \frac{\partial^2 \psi^m}{\partial r^2} \right|_{r=0} = 0 \quad , m \geq 1$$

These two last boundary conditions are not incompatible, and allow us to take into account flows that cross the rotation axis.

III. STEWARTSON LAYERS

A. Previous studies

The linear study of shear layers due to differential rotation of the walls has been done in the case of two concentric co-rotating disks [22], and in the case of two concentric differentially rotating spheres [23].

At first order, the flow is invariant along the direction of the rotation axis, and consists of a shear layer which is smoothing out the discontinuity. There are actually two nested layers (see fig. 1) with depth scaling like $E^{1/3}$ for the inner layer, and $E^{1/4}$ for the outer one. Note that the $1/3$ layer is not two-dimensional and smooth out the singularity in the Ekman pumping due to the outer layer. For the spherical shell case, the inner layer depth scaling is slightly modified ($E^{2/7}$), but the outer one remains the same. Thus, we can expect that the destabilization of the shear layer in both cases will be closely related. To study the destabilization of such a layer, we use our two-dimensional formalism, and eventually correct it for the presence of the $E^{1/3}$ -layer.

B. QG-model predictions

In the linear and stationnary regime, when the Rossby number is small, equation 14 reduces to a balance between the Ekman pumping term 15 and the interior viscosity :

$$2E^{1/2} \frac{\alpha}{2L} (\bar{u}_\phi - U_b) = E \left(\nabla^2 \bar{u}_\phi - \frac{\bar{u}_\phi}{r^2} \right) \quad (20)$$

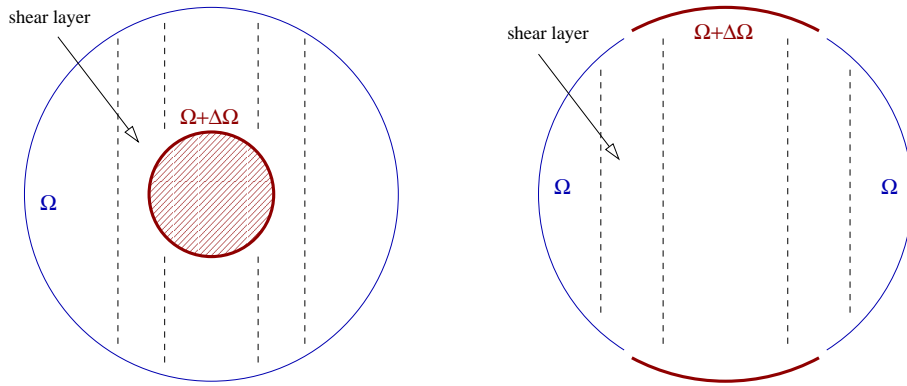


FIG. 2: Left, the spherical shell geometry, studied by [23]. Right, the split-sphere geometry this paper focus on.

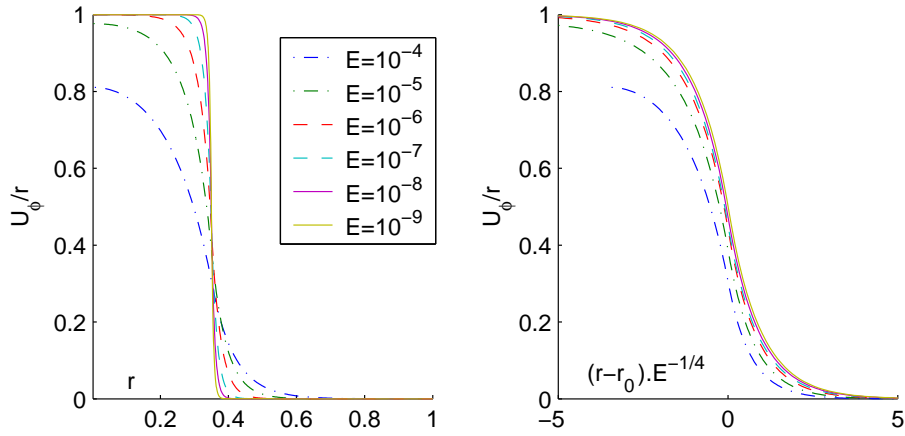


FIG. 3: Base flow showing the shear layer which scales with $E^{1/4}$ in the asymptotic low Ekman number regime, for $r_0 = 0.35$ in the split-sphere geometry.

which defines the Stewartson layer. Introducing Δ , the width of the Stewartson shear layer, we rewrite this equation in terms of order of magnitude :

$$E^{1/2} \alpha \sim E \frac{1}{\Delta^2} \quad (21)$$

leading to the proper scaling for the width of the Stewartson layer, in agreement with the results obtained by Stewartson.

$$\Delta \sim E^{1/4} \quad (22)$$

Note that the neglected non-linear terms are small if $Ro/\Delta \ll 1$.

C. Numerical results

1. Split-sphere

The split-sphere geometry consist of a sphere, split at a given radius r_0 (see fig. 2). We solve equation 20 in the frame rotating with the outer part at angular velocity Ω_0 , while the inner part rotates differentially at $\Delta\Omega$ (positive or negative). This linear problem is solved by a simple matrix inversion using a finite difference radial scheme with variable grid spacing. In this case, the boundary velocity U_b is a simple function, $U_b = r$ if $r < r_0$ and $U_b = 0$ if $r > r_0$.

The resulting shear layer for $r_0 = 0.35$ is shown on figure 3. Properly scaled, all these profiles can be superposed in the asymptotic small Ekman number regime. The size of the shear layer scales like $E^{1/4}$, as predicted by the scaling analysis. The asymptotic regime seems to be attained for $E < 10^{-6}$.

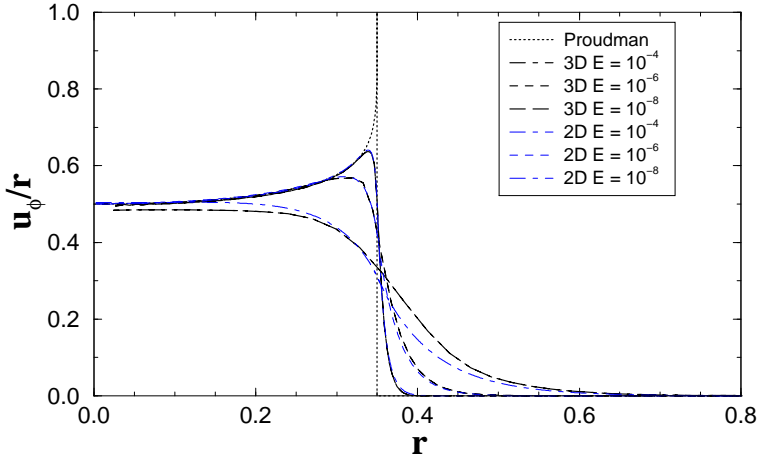


FIG. 4: Base flow for the spherical shell geometry ($r_0 = 0.35$). 2D refers to our model, Proudman is the asymptotic solution, and the other plots are 3D results from [7].

2. Spherical shell

The spherical shell (see fig. 2) geometry is the one studied originally by [20], and corresponds to a spherical-Couette flow. It is also of geophysical relevance because the core of the Earth is composed of a solid iron ball ($r_0 = 0.35$) surrounded by liquid iron. We have now a boundary velocity $U_b = r$ for the inner sphere, and $U_b = 0$ for the outer one. We reduce this problem to the upper half, assuming the equator is a symmetry plane. Note that the equation is now slightly different because we no longer have $L_+ = -L_- = L$.

The problem of the Stewartson layer in a spherical shell (including the $E^{1/3}$ -layer), has been addressed numerically by [7], with a full three dimensional code. We compare these results with the ones obtained with our model on figure 4. For $E = 10^{-4}$, discrepancies are quite important. However for $E = 10^{-6}$ and even better $E = 10^{-8}$, agreement between both results is good. This was expected because the QG-model is designed for these small Ekman number regimes. From these results we can also expect the $E^{1/3}$ -layer to play only a minor role at such small Ekman numbers. Note that we can compute very easily such profiles, for virtually any Ekman number, going very close to the asymptotic limit predicted by [20].

IV. ASYMPTOTIC STABILITY THRESHOLD

A. Scaling analysis

We perform a linear stability analysis on equation 4. Let $U(r) \mathbf{e}_\phi$ be the base velocity profile, solution of equation 20, and \mathbf{u} the perturbation. With

$$\Omega = \frac{\partial U}{\partial r} + \frac{U}{r}$$

the vorticity associated with $U(r)$, we find

$$\frac{\partial \omega}{\partial t} + Ro \left(u_r \frac{\partial \Omega}{\partial r} + \frac{U}{r} \frac{\partial \omega}{\partial \phi} \right) - (2 + Ro \Omega) \left\langle \frac{\partial u_z}{\partial z} \right\rangle = E \nabla^2 \omega \quad (23)$$

The assumption that $Ro/\Delta \ll 1$ implies that the local vorticity $Ro \Omega$ can also be neglected in the Coriolis term, giving a physical meaning to this approximation. We now introduce the frequency f of the disturbance, and its typical azimuthal wave length m . We will examine the two cases, with and without slope, but let us first examine the inertial terms, which don't depend on the vortex stretching term :

At the stability threshold, we expect these terms to be in balance :

$$\Delta^{-2} \sim m^2$$

This implies that the wavelength is determined by the thickness of the shear layer

$$m \sim \Delta^{-1} \sim E^{-1/4}$$

and also that Ekman friction and viscosity are of the same order of magnitude, which is the equilibrium that gave Δ (see §III).

1. Without slope

When there is no slope equation 10 gives

$$\left\langle \frac{\partial u_z}{\partial z} \right\rangle = -\frac{E^{1/2}}{2L} \omega \quad (24)$$

so that equation 23 gives in terms of order of magnitude :

$$\underbrace{mf}_{\text{shear}} + \underbrace{Ro \Delta^{-2}}_{\text{advection}} + \underbrace{\frac{Ro m^2}{L}}_{\text{Ekman friction}} \sim \underbrace{Em^3}_{\text{viscosity}}$$

With $m \sim E^{-1/4}$, the stability threshold is given by a balance between the non-linear forcing and the viscous damping :

$$Ro_c \sim E^{3/4}$$

which is consistent with the critical local Reynolds number theory for the shear layer [see 17]. For a wavy instability, the frequency f verifies $mf \sim Ro m^2$, and so

$$f \sim E^{1/2}$$

2. With slope

When the slope is important, $\frac{\partial u_z}{\partial z} = \beta u_r$, and so equation 23 gives the following balance :

$$\underbrace{mf}_{\text{shear}} + \underbrace{Ro \Delta^{-2}}_{\text{advection}} + \underbrace{\frac{Ro m^2}{2\beta}}_{\text{slope}} \sim \underbrace{Em^3}_{\text{viscosity}}$$

If again $m \sim E^{-1/4}$, the viscosity is negligible and the stabilization is due to the slope : the instability has to overcome the Proudman-Taylor constraint. As a matter of fact, from a balance between slope and forcing, we find

$$Ro_c \sim 2\beta E^{1/2}$$

For a time-dependant instability, the frequency f verifies $mf \sim 2\beta$, and

$$f \sim \frac{2\beta}{m}$$

which is the Rossby wave dispersion relation. In addition, we can check that the Ekman pumping, is again of the same order than internal viscous dissipation, and is thus negligible at the threshold.

Note that the obtained stability thresholds are low enough so that the assumption that $Ro/\Delta \ll 1$, which was used to derive equation 20, is valid for the stable shear layer and up to the stability threshold.

| E | Ro_c^R | m_c^R | Ro_c^S | m_c^S |
|---------------------|----------|---------|----------|---------|
| $1.1 \cdot 10^{-5}$ | 0.044 | 6-8 | 0.021 | 6 |
| $8.3 \cdot 10^{-6}$ | 0.032 | 6-8 | 0.017 | 6 |
| $5.6 \cdot 10^{-6}$ | 0.025 | 6-8 | 0.013 | 7 |

TABLE I: Comparison between the experimental results of [9] (denoted by R) and the numerical results we obtain (S) for the stability threshold.

| E | Ro_c^N | m_c^N | Ro_c^S | m_c^S |
|---------------------|----------|---------|----------|---------|
| $3.0 \cdot 10^{-5}$ | 0.050 | 5-6 | 0.048 | 5 |
| $6.0 \cdot 10^{-6}$ | 0.015 | 7-9 | 0.0145 | 8 |

TABLE II: Comparison between the experimental results of [17] (denoted by N) and the numerical results we obtain (S) for the stability threshold.

B. Numerical results

1. Flat container

We reproduce numerically the constant depth experiment done by [9]. The results of our linear calculation for the threshold is significantly lower than the experimental one, but in good agreement with the theory of [17]. The critical wave length are in good agreement, even above the stability threshold, as shown in table I. This suggest that the $E^{1/4}$ shear layer is correctly resolved.

To explain this discrepancy, [9] invoke the lack of the inner layer in the modelling of [17], which is also missing here. However, we can correct for it, as shown in section V B.

We also reproduce the experiment of [17], which has the particularity of having differential rotation only at the bottom, the top rotating at the mean angular velocity. This implies that the base flow has actually two shear layer, one beeing the Stewartson shear layer, the other beeing a parietal shear layer, attached to the outer boundary. Results are reported in table II and agree with the original experimental data, as well as with their numerical calculations.

2. Split-sphere geometry

Finally, we did the computation in the case of a split sphere. The problem is that the slope parameter β becomes very large near the equator. In fact, we can show that the Ekman pumping flow becomes dominant in an equatorial layer of width scaling like $E^{2/5}$. In this modified Ekman layer, the two-dimensional approximation certainly breaks down and our model is no longer valid.

The results for the stability threshold are given in table III and plotted in figure 5. They match the asymptotical scaling obtained previously, especially for small Ekman numbers. However significant deviations are observed including a difference between positive and negative Rossby numbers. This will be investigated in §V.

We expect the perturbation to be a Rossby wave. However, for negative Ro , ω_c is negative, which is not compatible with a Rossby wave. Looking more carefully, the instability develops in the outer region ($r > r_0$) for $Ro > 0$ and in the inner region ($r < r_0$) for $Ro < 0$, which is strongly advected by the base flow (see figure 3). We can correct for this advection effect, and the resulting data are shown on figure 5. This implies that the perturbation is a travelling Rossby wave in both cases.

Figure 6 shows the flow at the threshold for $E = 10^{-6}$. The radial features will be addressed in §VI.

3. Boundary conditions and viscosity

With the numerical code, we can test the behaviour of the stability threshold for different modifications in the model. Results are summarized in table IV. One can notice that the boundary condition (free-slip or no-slip) hardly affects the threshold, whereas the presence of Ekman friction has a visible effect, which seems to be less important at low Ekman number. Suppressing the viscosity lowers significantly the threshold, but it remains of the same order.

| E | Ro_c | m_c | ω_c | NR |
|------------|------------------------|-------|------------------------|------|
| 10^{-4} | $18.96 \cdot 10^{-2}$ | 2 | $11.4 \cdot 10^{-2}$ | 200 |
| | $-29.86 \cdot 10^{-2}$ | 2 | $-4.45 \cdot 10^{-2}$ | |
| 10^{-5} | $4.017 \cdot 10^{-2}$ | 5 | $9.886 \cdot 10^{-2}$ | 300 |
| | $-5.122 \cdot 10^{-2}$ | 4 | $-3.495 \cdot 10^{-2}$ | |
| 10^{-6} | $9.505 \cdot 10^{-3}$ | 10 | $5.428 \cdot 10^{-2}$ | 400 |
| | $-11.08 \cdot 10^{-3}$ | 8 | $-2.060 \cdot 10^{-2}$ | |
| 10^{-7} | $2.326 \cdot 10^{-3}$ | 18 | $2.689 \cdot 10^{-2}$ | 600 |
| | $-2.674 \cdot 10^{-3}$ | 15 | $-0.999 \cdot 10^{-2}$ | |
| 10^{-8} | $6.314 \cdot 10^{-4}$ | 33 | $1.388 \cdot 10^{-3}$ | 800 |
| | $-7.018 \cdot 10^{-4}$ | 31 | $-6.446 \cdot 10^{-3}$ | |
| 10^{-9} | $1.821 \cdot 10^{-4}$ | 63 | $7.505 \cdot 10^{-3}$ | 1200 |
| | $-1.938 \cdot 10^{-4}$ | 61 | $-3.844 \cdot 10^{-3}$ | |
| 10^{-10} | $5.357 \cdot 10^{-5}$ | 121 | $4.128 \cdot 10^{-3}$ | 1500 |
| | $-5.543 \cdot 10^{-5}$ | 119 | $-2.317 \cdot 10^{-3}$ | |

TABLE III: Linear stability threshold values for different Ekman numbers E . NR denotes the number of radial grid points used for the calculation. These values were obtained by QG numerical calculations with *no-slip boundary conditions* and including *Ekman friction*.

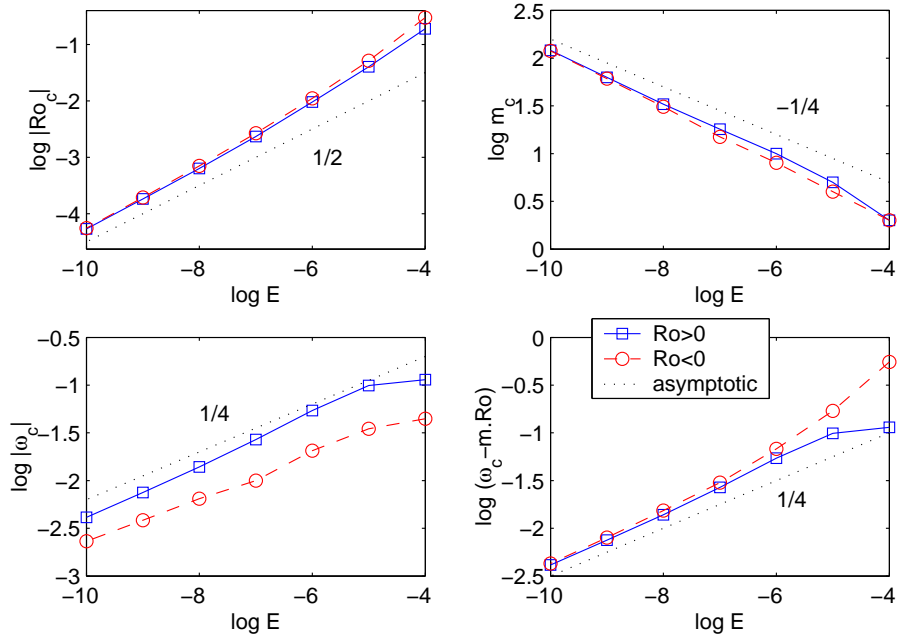


FIG. 5: Plot of the data from table III as a function of the Ekman number. The top-left plot represents the threshold; the top-right one shows the critical wave number; the bottom-left graph is the raw pulsation at the threshold, whereas the bottom-right one is corrected for advection effects.

Another effect of removing the viscosity is that the critical mode m_c is significantly higher, by a factor 1.3 to 1.4. The divergence correction we introduced seem to be really negligible at the threshold. In general, we can say that all models seem to converge when lowering the Ekman number.

4. Spherical shell geometry

The spherical shell is not tractable with the QG-model because β changes sign after going to infinity. This implies that Rossby waves will travel in opposite direction inside and outside the tangent cylinder.

We used the dynamo benchmark code [6] to perform a full 3D numerical calculation at $E = 10^{-4.5}$. The critical Rossby number we find $Ro_c = 0.16$ is in very good agreement with the experimental one.

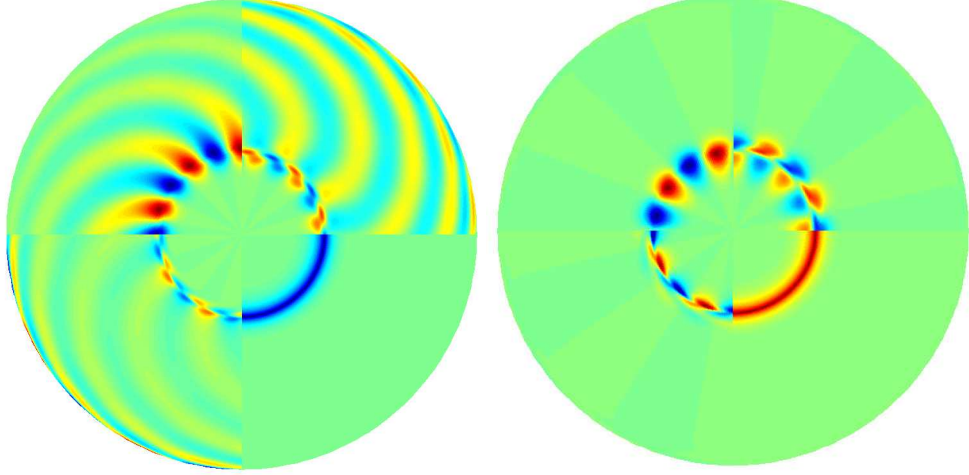


FIG. 6: Features of the flow at the threshold for $E = 10^{-6}$. The picture on the left is for $Ro > 0$, and the one on the right is for $Ro < 0$. On each picture, upper right corner shows the azimuthal velocity and upper left is the radial velocity. The lower left corner is the vertical vorticity field, and the lower right one is the differentiated angular velocity of the zonal flow, which shows the shear layer.

| E | ns, ep | $ns, ep0$ | $fs, ep0$ | $ns, ep, dv0$ | $ns, ep, vs0$ | $ns, ep, \times 2$ |
|-----------|----------|-----------|-----------|---------------|---------------|--------------------|
| 10^{-6} | 1.0 | 0.86 | 0.87 | 0.995 | 0.64 | 0.999 |
| 10^{-7} | 1.0 | 0.91 | 0.91 | 1.001 | 0.72 | 1.000 |
| 10^{-8} | 1.0 | 0.94 | 0.94 | 1.002 | 0.78 | 1.000 |

TABLE IV: Comparison between Ro_c of different numerical models. Values are the Ro_c obtained by a model divided by the reference Ro_c (ns, ep) for $Ro > 0$ at a given Ekman number. The models are referenced by ns and fs respectively for no-slip and free-slip boundary conditions, ep for the Ekman pumping, dv for horizontal divergence and vs for volume viscosity; $\times 2$ stands for calculation with doubled number of radial grid points. A 0 denotes the absence of this feature.

C. Experimental study

As far as we know, there is no spherical experiment looking for the destabilization of a Stewartson layer, so we build our own.

1. Experimental setup

An axysymmetric ellipsoidal container which is very close to a sphere, contains water and is rotated by a motor at variable angular speed Ω_0 . On this rotating frame, a small step-motor drives the inner axis differentially, at an angular velocity $\Delta\Omega$. On that axis, we can attach an inner sphere or two disks, which is more tractable numerically. Power and controls for the step-motor are passed from rotating frame into the lab-frame using a rotating electrical slip ring. All dimensions are reported on figure 7, and further details can be found in [18].

To determine the stability threshold, we use a flake solution (Kalliroscope AQ 1000) in combination with a projected light slice. This allows us to see the shear-field in a plane. When the shear-field is steady, we assume that the flow is stable, and when the shear becomes unsteady (oscillations in time), the flow is unstable. A few pictures of the observed patterns are reproduced on figure 8. Many operators have done some calibration experiments to test the high sensitivity on the determination of the onset.

2. Experimental results

The threshold is obtained for different values of the Ekman number with two geometries and reported in tables V and VI, for prograde differential rotation. Results for the stability threshold are summarized on figure 9.

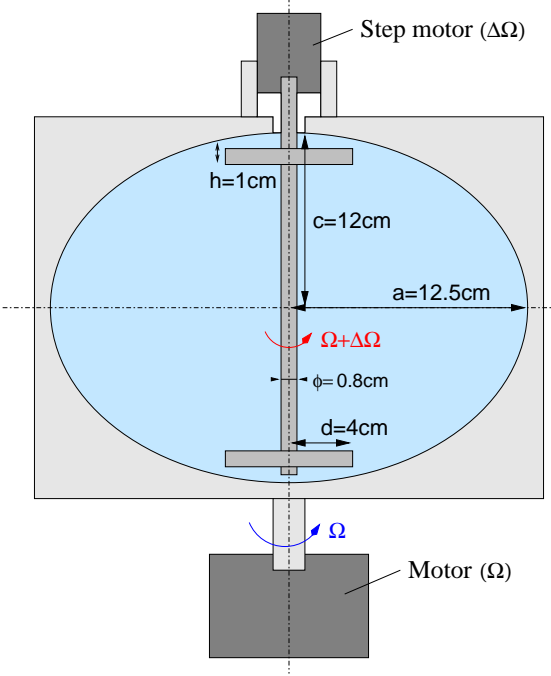


FIG. 7: Sketch of the experimental setup with disks geometry. Spherical shell geometry is obtained by replacing the disks by a sphere on the inner rotating axis.

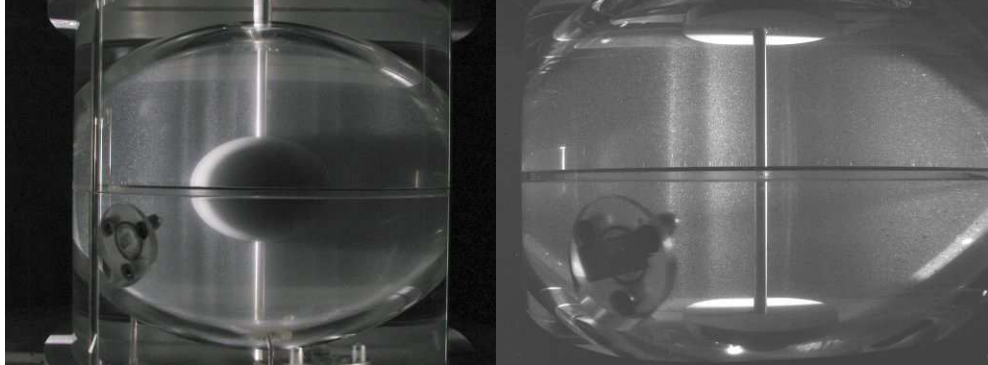


FIG. 8: Instabilities near the threshold as seen in our experiments (for $E \simeq 10^{-5}$). The features shown by the flakes are vertical, supporting the QG-approximation for our model.

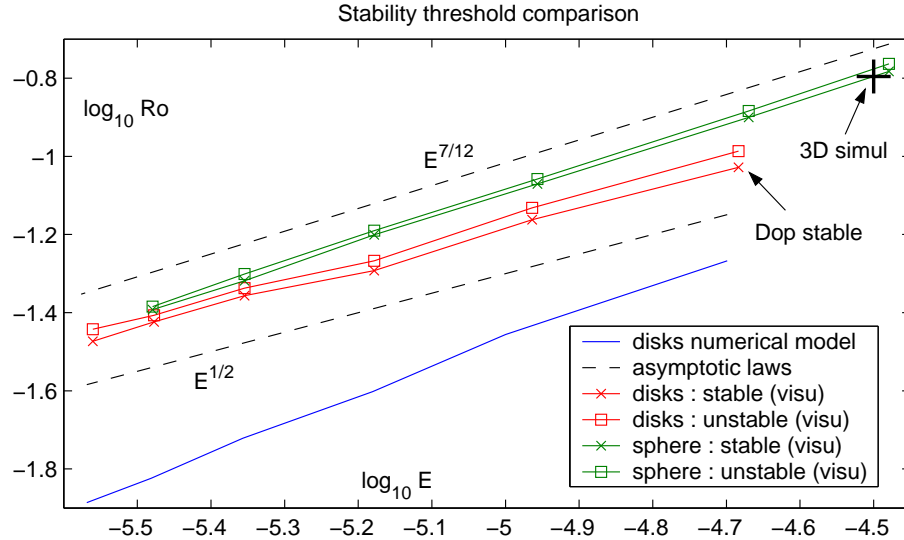
The disk case seem to agree with the $E^{1/2}$ scaling, whereas the sphere case is significantly steeper. Both geometries are very close suggesting that the same mechanism is at work. The numerical calculations for the disk model give too low stability thresholds. This is probably because of the jump in height in the disk experiment that is not present in the numerical model. Another possible cause could be the effect of the $E^{1/3}$ -layer which is not present in the disks numerical model. This will be investigated in §VB

For both numerical and experimental results we observe significant discrepancies with the asymptotic laws, even with relatively small Ekman numbers. The next section will consider finer effects to correct the asymptotic laws.

| Ω (rpm) | E | stable Ro | unstable Ro |
|----------------|--------------|-------------|---------------|
| 20.9 | 3.310^{-5} | 0.330 | 0.345 |
| 32.5 | 2.110^{-5} | 0.251 | 0.261 |
| 62.8 | 1.110^{-5} | 0.170 | 0.175 |
| 104.7 | 6.610^{-6} | 0.126 | 0.129 |
| 157.1 | 4.410^{-6} | 0.096 | 0.100 |
| 209.4 | 3.310^{-6} | 0.081 | 0.083 |
| 261.8 | 2.710^{-6} | 0.070 | 0.072 |

TABLE V: Stability threshold experimental data obtained for the spherical shell geometry, in water ($\nu = 10^{-6}$ m²/s)

| Ω (rpm) | E | stable Ro | unstable Ro |
|----------------|--------------|-------------|---------------|
| 33.5 | 2.110^{-5} | 0.094 | 0.103 |
| 63.9 | 1.110^{-5} | 0.069 | 0.074 |
| 104.7 | 6.610^{-6} | 0.051 | 0.054 |
| 157.1 | 4.410^{-6} | 0.044 | 0.046 |
| 208.4 | 3.310^{-6} | 0.038 | 0.039 |
| 252.4 | 2.810^{-6} | 0.034 | 0.036 |

TABLE VI: Stability threshold experimental data obtained for the disks geometry, in water ($\nu = 10^{-6}$ m²/s)FIG. 9: Experimental determination of the stability threshold for two geometries, compared with asymptotic laws and numerical calculations. *Dop stable* stands for a point that was checked by Doppler measurements to be stable. *3D simul* is the stability threshold obtained by a full 3D simulation.

V. CORRECTIONS TO THE ASYMPTOTIC LAWS

A. Finite Rossby number effect

From equation 4, we write the linear equation for small perturbations around the axisymmetric shear flow U of vorticity Ω .

$$\frac{\partial \omega}{\partial t} + Ro \left(u_r \frac{\partial \Omega}{\partial r} + \frac{U}{r} \frac{\partial \omega}{\partial \phi} \right) - (2 + Ro\Omega) \left\langle \frac{\partial u_z}{\partial z} \right\rangle = E \nabla^2 \omega \quad (25)$$

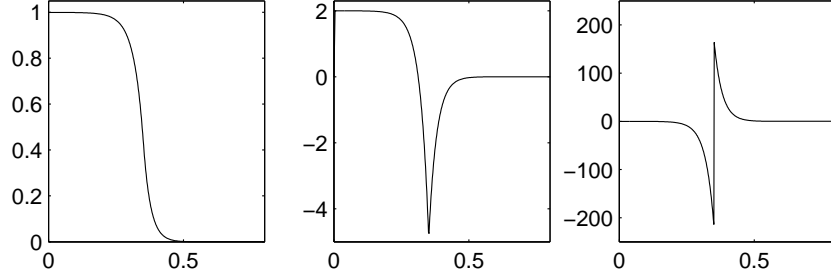


FIG. 10: Base axisymmetric flow profiles, as function of radius r for $E = 10^{-6}$ and a split-sphere geometry with $r_0 = 0.35$. From left to right : rotation velocity U/r , vorticity Ω , and radial derivative of vorticity $\frac{\partial\Omega}{\partial r}$.

We are looking for solutions of the form $\Psi(r, \phi, t) = e^{i(m\phi + \lambda t)}\psi(r)$. We use the Ψ formulation introduced in section II F, but without the β -terms to keep simpler expressions. Ignoring Ekman friction and viscosity, we obtain

$$\left(\lambda + \frac{im}{r}RoU\right)\omega[\psi] = \left((2 + Ro\Omega)\beta - Ro\frac{\partial\Omega}{\partial r}\right)\frac{im}{r}\psi \quad (26)$$

Multiplying by $\psi^*L(r)r$ and integrating over r we have

$$\int_0^1 \omega[\psi]\psi^*Lr dr = \int_0^1 \frac{(2 + Ro\Omega)\beta - Ro\frac{\partial\Omega}{\partial r}}{\lambda + \frac{im}{r}RoU} im|\psi|^2 L dr \quad (27)$$

Expanding the left hand side of this equation, and integrating by part, we obtain

$$\int_0^1 \psi^* \left(\frac{m^2}{r^2}\psi - \frac{1}{r}\frac{\partial}{\partial r} \left(r\frac{\partial\psi}{\partial r} \right) \right) Lr dr = \int_0^1 \frac{m^2}{r^2}\psi\psi^*Lr dr + \left[\psi^*\frac{\partial\psi}{\partial r} \right]_0^1 - \int_0^1 \left| \frac{\partial\psi}{\partial r} \right|^2 Lr dr \quad (28)$$

and from the boundary conditions the border term vanishes, leading to

$$\int_0^1 \left(\frac{m^2}{r^2}|\psi|^2 + \left| \frac{\partial\psi}{\partial r} \right|^2 \right) Lr dr = \int_0^1 \frac{im|\psi|^2((2 + Ro\Omega)\beta - Ro\frac{\partial\Omega}{\partial r})(\lambda^* - \frac{im}{r}RoU)}{|\lambda + \frac{im}{r}RoU|^2} L dr \quad (29)$$

With $\Re(\lambda)$ the real part of the complex number λ , the imaginary part of this equation gives

$$0 = \Re(\lambda^*) \int_0^1 \frac{|\psi|^2((2 + Ro\Omega)\beta - Ro\frac{\partial\Omega}{\partial r})}{|\lambda + \frac{im}{r}RoU|^2} L dr \quad (30)$$

For a mode to be unstable, we need $\Re(\lambda^*) \neq 0$, which means that there is an r for which

$$(2 + Ro\Omega)\beta - Ro\frac{\partial\Omega}{\partial r} = 0 \quad (31)$$

Note that using the complete pseudo-stream function given in section II F leads to the same result. As a consequence, the determination of the stability threshold will not be affected by using the small slope approximation, as it is usually done for the thermal convection case [see 4].

The critical Rossby number Ro_c that will satisfy 31 will be obtained for the maximum value of $|\frac{\partial\Omega}{\partial r}|$. We must now study the sign of the terms in equation 31. β is negative for L decreasing with r . Ω is essentially negative in the shear zone, and $\frac{\partial\Omega}{\partial r}$ is peaked in the shear zone, with roughly equal positive and negative peak values (see figure 10). Reminding that $|Ro| \ll 1$, and separating positive (Ro^+) and negative (Ro^-) values of the Rossby number, we may write

$$(2 \mp |Ro_c^\pm| |\Omega|) |\beta| = |Ro_c^\pm| \left| \frac{\partial\Omega}{\partial r} \right| \quad (32)$$

from which we get the critical Rossby number :

$$|Ro_c^\pm| = \frac{2|\beta|}{\left| \frac{\partial\Omega}{\partial r} \right| \pm |\Omega\beta|} \quad (33)$$

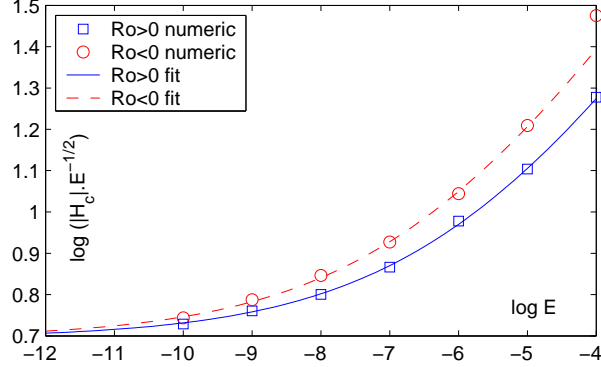


FIG. 11: Stability threshold data from numerical simulations for both positive and negative differential rotation and their corresponding fit using the linear theory described in §VA.

We must now take care of what value of β comes into this expression. Actually, the shear layer samples the values of β about Δ around the split radius r_0 . We will assume that the largest sampled value of $|\beta|$ is the one that enters the equation, because the perturbation has to overcome that slope.

Assuming Δ is small enough to use a Taylor expansion

$$|\beta(r_0 \pm \Delta)| = |\beta_0| \pm \Delta \left(\frac{\partial |\beta|}{\partial r} \right)_0$$

we obtain

$$|Ro^\pm| = 2\Delta^2 \left(|\beta_0| + \Delta \left(\left(\frac{\partial |\beta|}{\partial r} \right)_0 \mp \beta_0^2 \right) \right) \quad (34)$$

keeping only the first order correction in Δ .

With $\Delta \sim E^{1/4}$, we expect a law of the form

$$|Ro^\pm| = a E^{1/2} \left(1 + c^\pm E^{1/4} \right) \quad (35)$$

Figure 11 shows that this law fits quite well the threshold obtained by numeric simulation for the split-sphere geometry (table III) with

$$a = 4.95 \quad c^+ = 28 \quad c^- = 40$$

It also explains the difference between positive and negative Rossby numbers. This asymmetry between positive and negative differential rotation has never been pointed out in the previous linear theories.

B. Effect of the $E^{1/3}$ layer

The asymptotic base solution obtained by [22] contains a $E^{1/3}$ (fig. 1) shear layer, located inside the main geostrophic $E^{1/4}$ layer. This layer is not z -invariant, and is hence excluded by our QG-model. The base linear profiles given by our QG-model (without this inner layer) are represented on figure 10. As we can see, the second radial derivative of the flow is discontinuous. The effect of the $E^{1/3}$ layer is to smooth out this discontinuity (see [15]), which directly affects the stability threshold.

A simple way to take this effect into account is to average the flow around the discontinuity. Neglecting the curvature effects, we have

$$\frac{\partial \Omega}{\partial r} \sim \frac{1}{\Delta^2} e^{-r/\Delta}$$

The average value around $r = 0$ in a layer of width $\Delta' \sim E^{1/3}$ is then, at the first non-vanishing order :

$$\left\langle \frac{\partial \Omega}{\partial r} \right\rangle \sim \frac{1}{\Delta^2} \left(1 - \frac{\Delta'}{2\Delta} \right) \quad (36)$$

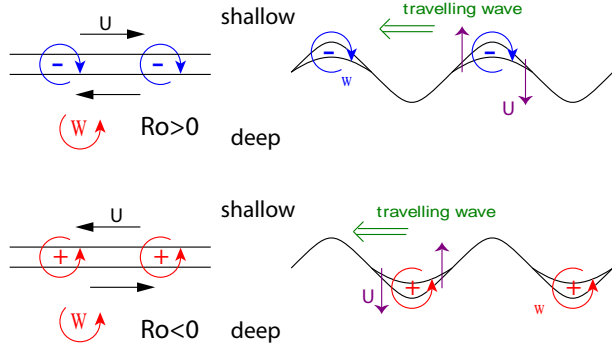


FIG. 12: Instability mechanism

Which means that there is a $\Delta'/\Delta \sim E^{1/12}$ correction for the $E^{1/2}$ law. More precisely, putting 36 back into 33, we find

$$|Ro_c^\pm| = a E^{1/2} \left(1 + b E^{1/12} + c^\pm E^{1/4} \right) \quad (37)$$

b is the correction due to the $E^{1/3}$ layer, and we have $b = 0$ for QG-calculations but we expect $b > 0$ for the real flow, so that the threshold is higher than predicted by numerical simulations. In fact, the $E^{1/3}$ -layer reduces the maximum values of $|\frac{\partial \Omega}{\partial r}|$ by smoothing the singularity. This implies an increased critical Rossby number. c^\pm is the finite Rossby number correction obtained in §VA, and we expect $c^+ < c^-$. All these coefficient obviously depend on the geometry of the container.

Note that equation 37 asymptotically reduces to $a E^{1/2}$, but the $E^{1/12}$ correction may be important, even for very small values of E .

1. Back on the experiments

Looking carefully at figure 9, one can notice different things. On one hand, the disks case is well explained by an $E^{1/2}$ law, showing that the effect of the $E^{1/3}$ -layer may be unimportant. On the other hand, an $E^{7/12}$ law is in good agreement with the stability threshold for the spherical shell geometry, suggesting that the effect of the $E^{1/3}$ -layer may be more important in that configuration. This latter case is compared to full 3D numerical simulations, whereas the disk case has been modelled using our QG-model, unable to take the jump at the disks edges (see fig. 7) into account. This may be responsible for the observed discrepancies.

The result of [11], $Ro_c = 29E^{0.6}$ for a flat container is close to $E^{7/12}$. A slightly tilted top or bottom could explain such result, which is significantly different from the $E^{3/4}$ law found by [17] and [9].

VI. RADIAL SCALINGS AT THE ONSET

A. Dependance on the sign of the Rossby number

We can observe on figure 6 that the instability develops in the inner region of the tangent cylinder for $Ro < 0$, and in the outer one for $Ro > 0$. This is explained by a β -effect on the instability, as represented on figure 12.

A vorticity sheet (the internal shear layer) is perturbed. The fluid is slightly radially displaced from its equilibrium position. However, mass conservation and the Kelvin theorem impose that a column displaced toward a deeper region is contracted and its vorticity gets stronger. We are in a low Rossby regime, so that the total vorticity is always positive ($2\Omega_0 + \omega > 0$). If $\omega > 0$ the local vorticity gets amplified, and if $\omega < 0$ it is damped. This is exactly the conservation of potential vorticity.

For $Ro > 0$, the vorticity sheet is negative and thus the perturbation is damped in the deeper interior region, whereas it is amplified in the outer shallow region. For $Ro < 0$, it is the opposite. In both cases, the amplified vorticity will induce a flow which induces a drift of the pattern in the prograde direction (as for any Rossby wave).

B. Approximations and assumptions

On figure 6 the perturbation of the shear layer spreads across the whole volume whereas in the thermal convection case [see 8] it is radially localized. In this section we derive a simple heuristic model that predict all these properties *outside the shear layer*.

To simplify our study, we make a few approximations :

- we neglect the curvature;
- we drop the viscous dissipation term, but keep the Ekman friction;
- we assume small forcing, ignoring the local vorticity term.

The curvature may be negligible if the scales involved are small enough. Looking at the results from section V, we expect the scales to shrink while lowering the Ekman number. Thus, we replace the angular variable ϕ by y . Dropping the viscous term lowers the order of the differential equation and make it easier to handle. Numerical simulations with no viscous term or an artificially weakened viscous term show that the structure stays very similar. In addition, the threshold is expected to be only slightly affected in the asymptotic regime, as suggested by the results of table IV. This is because the Ekman pumping does a comparable job. Finally, we can neglect the local vorticity term because in the linear stability case it is a higher order effect, as shown in section V A. We end up with

$$\frac{\partial \omega}{\partial t} + Ro \left(U \frac{\partial \omega}{\partial y} + u_r \frac{\partial \Omega}{\partial r} \right) = 2 \left\langle \frac{\partial u_z}{\partial z} \right\rangle \quad (38)$$

The expression of the Ekman friction involves several terms. We will only keep the vorticity contribution, so that

$$\left\langle \frac{\partial u_z}{\partial z} \right\rangle \simeq \beta u_r - \alpha E^{1/2} \omega \quad (39)$$

where α is the geometrical factor for the Ekman friction term, and for a sphere $\alpha = (1 - r^2)^{-3/4}$.

We now assume a perturbation of the form

$$\Psi(r, y, t) = \psi(r) e^{i(ky - \omega t)}$$

and we obtain

$$\left(-i\omega + RoUik + E^{1/2}\alpha \right) \left(k^2 - \frac{\partial^2}{\partial r^2} \right) \psi + \left(Ro \frac{\partial \Omega}{\partial r} - 2\beta \right) ik\psi = 0 \quad (40)$$

In a more convenient form, we can write

$$\frac{\partial^2 \psi}{\partial r^2} = k^2 \left(1 + \frac{1}{k} \frac{(2\beta - Ro \frac{\partial \Omega}{\partial r})(\omega - RoUk - iE^{1/2}\alpha)}{(\omega - RoUk)^2 + E\alpha^2} \right) \psi \quad (41)$$

C. Outer part, large β

In the outer part the base velocity profile U is vanishing, as well as $\frac{\partial \Omega}{\partial r}$. This simplifies the previously established relation 41 :

$$\frac{\partial^2 \psi}{\partial r^2} = k^2 \left(1 + \frac{2\beta}{k} \frac{\omega - iE^{1/2}\alpha}{\omega^2 + E\alpha^2} \right) \psi \quad (42)$$

In the case of small Ekman number, $E\alpha^2$ is negligible compared to $\omega^2 \sim E^{1/2}$, but we have to keep the small imaginary part. We now set

$$\gamma = k \left| 1 + \frac{2\beta}{k\omega} \right|^{1/2}$$

If $|2\beta| \gg 1$, we can rewrite 42 as

$$\frac{\partial^2 \psi}{\partial r^2} = -\gamma^2 \left(1 - \frac{2i\beta E^{1/2}\alpha}{k\omega^2 + 2\beta\omega}\right) \psi \quad (43)$$

and the solution for constant α and β is of the form

$$\psi = \exp\left(\pm\gamma\frac{\beta E^{1/2}\alpha}{k\omega^2 + 2\beta\omega}r\right) \exp(\pm i\gamma r)$$

This implies a rapid oscillation of typical length scale γ

$$\gamma \sim k\sqrt{|2\beta|} \quad (44)$$

modulated by a slow exponential decay with typical length scale δ given by

$$\delta \sim \gamma^{-1} E^{-1/2} \alpha^{-1} \omega \quad (45)$$

Inside this envelope, the radial length scale γ^{-1} of the perturbation decreases when β increases. This results from the spiraling.

Using the scalings for the Stewartson layer instability $k \sim E^{-1/4}$ and $\omega \sim E^{1/4}$, relation 45 leads to

$$\delta \sim (2|\beta|)^{-1/2} \alpha^{-1} E^0 \quad (46)$$

which implies that the radial extension of the perturbation is independent of E . This is a fundamental difference with the thermal convection case investigated by [24] and [12] where the scaling $k \sim E^{-1/3}$ and $\omega \sim E^{1/3}$ implies

$$\delta \sim (2|\beta|)^{-1/2} \alpha^{-1} E^{1/6} \quad (47)$$

which corresponds to a slowly decaying radial extension when decreasing E . Note that Yano and Jones *et al.* dropped the $E^{1/2}$ pumping flow, but kept the volume viscosity instead.

D. Inner part, small β

The inner part behaves exactly as the outer one, replacing ω by $\omega - RoUk$. For a spherical shell it corresponds to the small β case.

If $|2\beta| < k\omega$, we can rewrite 42 as

$$\frac{\partial^2 \psi}{\partial r^2} = \gamma^2 \left(1 - \frac{2i\beta E^{1/2}\alpha}{k\omega^2 + 2\beta\omega}\right) \psi \quad (48)$$

which actually exchanges the length scale of the exponential decay and of the oscillation compared to the outer region. The solution for constant α and β is then

$$\psi = \exp(\pm\gamma r) \exp\left(\mp i\gamma\frac{\beta E^{1/2}\alpha}{k\omega^2 + 2\beta\omega}r\right)$$

which is an exponential decay of characteristic length γ^{-1} , inside which there are much larger length scale oscillations, which cannot be detected.

For the Rossby wave, we have $\omega \sim k^{-1}$, so that $\gamma \sim k$, with a correction independent of E . This shows that in the small β case the critical mode has a radial extension comparable to its azimuthal scale.

E. Numerical results

We show on figure 13 a fixed ϕ vorticity profile. It shows that the vorticity gets amplified by the decreasing depth as approaching the equator, while the spatial frequency of the oscillations increases, in agreement with equation 44. In addition even when decreasing E , the perturbation seems to spread across the whole depth of the tank, as predicted by the scaling 46.

The scaling 44 is observed quantitatively in numerical simulations as shown on figure 14. On this curves we can also see the effect of the equatorial boundary, which modifies the scaling. We also performed numerical calculations with β independent of r . In that case there is no spiraling.

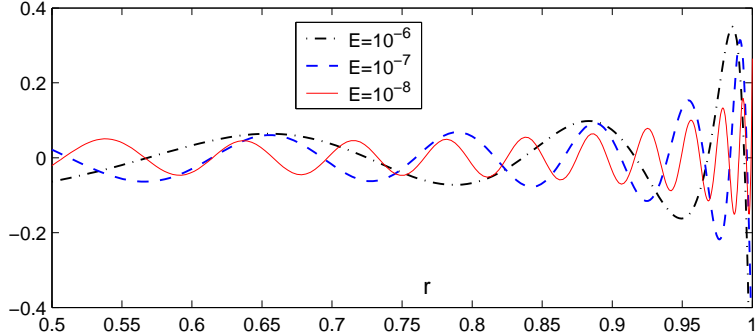


FIG. 13: Vorticity profile at fixed ϕ at the stability threshold for $Ro > 0$ in the outer region.

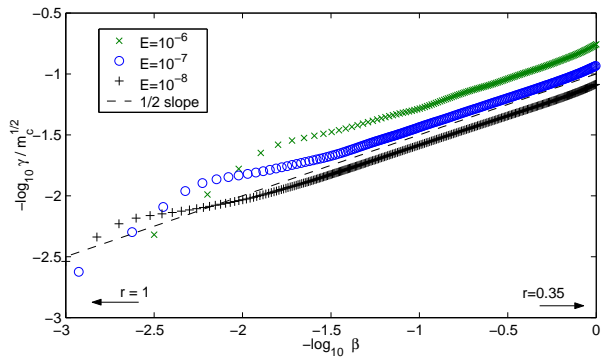


FIG. 14: Evolution of the radial size (evaluated using spatial derivation) of the unstable mode near the equatorial singularity for the split-sphere geometry. All these curves exhibit a wide range of slope $1/2$, which is the expected trend to cancel phase-mixing. Near the equatorial boundary ($r = 1$) this scaling is no longer valid.

VII. DISCUSSION AND CONCLUSION

In this study, we give a complete insight into the instability of a Stewartson shear layer.

The QG-model with the new pseudo-stream function formalism is designed for finite slopes, and is easy to implement. Despite failing to describe the $E^{1/3}$ -layer, it has proven to be a good tool for numerical experiments to reach very low Ekman numbers. It can also be used for non-linear calculations as long as the quasi-geostrophic hypothesis stands, and may be useful for future ocean and planetary interior models.

Our model allows us to compare flat top and bottom geometry with geometries containing a slope. Two different stabilizing processes are at work, leading to different balance and scalings.

Combining theoretical, numerical and experimental approach allowed us to show how the presence of the $E^{1/3}$ -layer affects the threshold, and to propose a new asymptotic scaling (eq. 37), which seem to be accurate up to relatively high Ekman numbers ($E \leq 10^{-5}$). It can be noted that the previous $E^{1/2}$ asymptotic scaling is only valid for very small Ekman numbers ($E \leq 10^{-8}$) that are difficult to obtain in laboratory experiments, and that the Ekman pumping plays a significant role, even at very low Ekman numbers.

The radial structure shows similarities with thermal convection as well as fundamental differences. In particular, if the global structure of the flow is quite similar to the spiraling flow of Busse, the radial extension of the instability is surprisingly independent of the Ekman number.

The non-linear and turbulent regime has to be investigated, by means of numerical calculations and quantitative velocity measurement in experiments. We also expect these flow to induce magnetic field. Future sodium experiments, as well as dynamo calculations will shed some light on this process.

Acknowledgments

Most of the computations presented in this paper were performed at the Service Commun de Calcul Intensif de l'Observatoire de Grenoble (SCCI).

We wish to thank Dominique Jault for stimulating discussions about this work. We are also grateful to Natalia Bezaeva, Daniel Brito, Jean-Paul Masson and Henri-Claude Nataf for their help in running the experiment. This work was funded by the French Ministry of Research and by the program *Intérieur de la Terre* of the CNRS/INSU.

APPENDIX A: EKMAN PUMPING IN A SPHERE

The Ekman pumping flow is given by [10]

$$\mathbf{u} \cdot \mathbf{n}|_{\pm L} = \frac{E^{1/2}}{2} \mathbf{n} \cdot \nabla \wedge \left(\frac{\mathbf{n} \wedge \mathbf{u} \mp \mathbf{u}}{\sqrt{|\mathbf{n} \cdot \mathbf{e}_z|}} \right) \quad (\text{A1})$$

with \mathbf{n} the *outward* unit vector normal to the surface and \mathbf{u} the velocity jump between the geostrophic interior and the boundaries. This Ekman pumping flow is the next order term in the $E^{1/2}$ development, and is deduced from the quasi-geostrophic, 0-order flow. However, it has a dynamic action on that flow, and is thus important for the dynamics of the system. For simplicity we assume that the boundaries are at rest in the rotating frame. It is straightforward to apply the result to moving boundaries by replacing the velocity by the jump in velocity.

1. Spherical coordinate system

We can separate this

$$\frac{1}{2} E^{1/2} \left(\underbrace{\mathbf{n} \cdot \nabla \wedge \left(\frac{\mathbf{n} \wedge \mathbf{u}}{\sqrt{|\mathbf{n} \cdot \mathbf{e}_z|}} \right)}_a \mp \underbrace{\mathbf{n} \cdot \nabla \wedge \left(\frac{\mathbf{u}}{\sqrt{|\mathbf{n} \cdot \mathbf{e}_z|}} \right)}_b \right)$$

We now use the spherical coordinate system (ρ, θ, ϕ) to develop that expression, because it is the natural one for that boundary layer ($\mathbf{n} = \mathbf{e}_\rho$). Term a reduces to

$$a = |\cos \theta|^{-1/2} \left(\pm \frac{|\tan \theta|}{2\rho} u_\theta - \frac{\partial u_\rho}{\partial \rho} - \frac{2}{\rho} u_\rho \right)$$

and term b can be written as

$$b = |\cos \theta|^{-1/2} \left(\pm \frac{|\tan \theta|}{2\rho} u_\phi + \omega_\rho \right)$$

On the boundary, we have $\rho = 1$, and so

$$\mathbf{u} \cdot \mathbf{n}|_{\pm L} = \frac{E^{1/2}}{2 |\cos \theta|^{1/2}} \left(\frac{|\tan \theta|}{2} (\pm u_\theta - u_\phi) \pm \omega_\rho - 2u_\rho - \frac{\partial u_\rho}{\partial \rho} \right) \quad (\text{A2})$$

2. QG-model flow

We now assume the use of our QG approximation described in §II. We need to translate A2 into cylindrical coordinate system (r, ϕ, z) . We have

$$\begin{aligned} \rho \sin \theta &= r & \rho \cos \theta &= z \\ u_\theta &= u_r \cos \theta - u_z \sin \theta & u_\rho &= u_r \sin \theta + u_z \cos \theta \end{aligned}$$

$$\frac{\partial}{\partial \rho} = \frac{\partial r}{\partial \rho} \frac{\partial}{\partial r} + \frac{\partial z}{\partial \rho} \frac{\partial}{\partial z} = \sin \theta \frac{\partial}{\partial r} + \cos \theta \frac{\partial}{\partial z}$$

Furthermore, u_r and u_ϕ are z -independent, and u_z is a linear function of z (see section II D) :

$$u_z = z \frac{-r}{1-r^2} u_r(r, \phi) \quad (\text{A3})$$

We find

$$\frac{\partial u_\rho}{\partial \rho} = \frac{-2r}{1-r^2} u_r \quad (\text{A4})$$

We also need to develop ω_ρ :

$$\omega_\rho = \omega_z \cos \theta + \omega_s \sin \theta$$

where ω_r is given by

$$\omega_r = \frac{1}{r} \frac{\partial u_z}{\partial \phi} = \frac{-z}{1-r^2} \frac{\partial u_r}{\partial \phi}$$

and finally

$$\begin{aligned} \mathbf{u} \cdot \mathbf{n}|_{\pm L} = & \frac{E^{1/2}}{2(1-r^2)^{1/4}} \left(\frac{-r}{2(1-r^2)^{1/2}} u_\phi + \frac{5}{2} \frac{r}{1-r^2} u_r \right. \\ & \left. - (1-r^2)^{1/2} \left(\omega_z - \frac{r}{1-r^2} \frac{\partial u_r}{\partial \phi} \right) \right) \end{aligned} \quad (\text{A5})$$

This expression can be treated just like the 0-order no-slip boundary condition :

$$\mathbf{u} \cdot \mathbf{n}|_{\pm L} = r u_r \pm \sqrt{1-r^2} u_z$$

from which we deduce u_z at the top and bottom boundary

$$\pm u_z|_{\pm L} = (1-r^2)^{-1/2} (\mathbf{u} \cdot \mathbf{n}|_{\pm L} - r u_r)$$

and from the linear z -dependence of u_z we obtain

$$\begin{aligned} \frac{\partial u_z}{\partial z} = & \frac{E^{1/2}}{2(1-r^2)^{3/4}} \left(-\omega_z + \frac{r}{1-r^2} \left(\frac{\partial u_r}{\partial \phi} - \frac{1}{2} u_\phi \right) + \frac{5r}{2(1-r^2)^{3/2}} u_r \right) \\ & + \frac{-r}{1-r^2} u_r \\ = & E^{1/2} \cdot P(u_r, u_\phi, r) + \beta u_r \end{aligned} \quad (\text{A6})$$

It has to be emphasized that this results from a development in $E^{1/2}$, which is no more valid when approaching the equator.

3. Validity

In the expression A7, we have an order $E^{1/2}$ and order 1 term. The development is no more valid when these two terms are of the same order of magnitude. Setting $r = 1 - \epsilon$, we have $1 - r^2 \sim 2\epsilon$. Keeping the dominant terms in $1/\epsilon$, the limit of validity is given by

$$\frac{E^{1/2}}{2(2\epsilon)^{3/4}} \frac{5}{2} \frac{1}{(2\epsilon)^{3/2}} u_r \sim \frac{1}{2\epsilon} u_r$$

from which we get

$$\epsilon \sim \frac{1}{2} \left(\frac{5}{4} \right)^{4/5} E^{2/5} \quad (\text{A7})$$

which shows the $E^{2/5}$ singularity on the equator [see 21]. The angular extension is easily obtained from geometrical considerations :

$$s = \cos \delta\theta \sim 1 - \delta\theta^2/2 \sim 1 - \epsilon$$

so that $\delta\theta = (2\epsilon)^{1/2}$ and

$$\delta\theta \sim E^{1/5} \quad (\text{A8})$$

[1] ANDEREK, C. D., LIU, S. & SWINNEY, H. L. 1986 Flow regimes in a circular couette system with independently rotating cylinders. *J. Fluid Mech.* **164**, 155–183.

[2] AUBERT, J., GILLET, N. & CARDIN, P. 2003 Quasigeostrophic models of convection in rotating spherical shells. *Geochem. Geophys. Geosyst.* **4**(7), 1052.

[3] BUSSE, F. 1968 Shear flow instabilities in rotating systems. *J. Fluid Mech.* **33**, 577–589.

[4] BUSSE, F. 1970 Thermal instabilities in rapidly rotating systems. *J. Fluid Mech.* **44**, 441–460.

[5] CARDIN, P., BRITO, D., JAULT, D., NATAF, H.-C. & MASSON, J.-P. 2002 Towards a rapidly rotating liquid sodium dynamo experiment. *Magnetohydrodynamics* **38**, 177–189.

[6] CHRISTENSEN, U., AUBERT, J., CARDIN, P., DORMY, E., GIBBONS, S., GLATZMAIER, G., GROTE, E., HONKURA, Y., JONES, C., KONO, M., MATSUSHIMA, M., SAKURABA, A., TAKAHASHI, F., TILGNER, A., WICHT, J. & ZHANG, K. 2001 A numerical dynamo benchmark. *Phys. Earth Planetary Interiors* **128**, 25–34.

[7] DORMY, E., CARDIN, P. & JAULT, D. 1998 MHD flow in a slightly differentially rotating spherical shell, with conducting inner core, in a dipolar magnetic field. *Earth. Planet. Sc. Lett.* **160**, 15–30.

[8] DORMY, E., SOWARD, A., JONES, C., JAULT, D. & CARDIN, P. 2003 The onset of thermal convection in rotating spherical shells. *accepted for publication in JFM*.

[9] FRÜH, W.-G. & READ, P. L. 1999 Experiments on a barotropic rotating shear layer. part 1. instability and steady vortices. *J. Fluid Mech.* **383**, 143–173.

[10] GREENSPAN, H. P. 1968 *The theory of rotating fluids*. Breukelen Press.

[11] HIDE, R. & TITMAN, C. 1967 Detached shear layers in a rotating fluid. *J. Fluid Mech.* **29**, 39–60.

[12] JONES, C. A., SOWARD, A. M. & MUSSA, A. I. 2000 The onset of thermal convection in a rapidly rotating sphere. *J. Fluid Mech.* **405**, 157–179.

[13] KISS, A. E. 2003 A modified quasigeostrophic formulation for weakly nonlinear barotropic flow with large-amplitude depth variations. *Ocean Model.* **5**, 171–191.

[14] VAN DE KONIJNENBERG, J. A., NIELSEN, A. H., RASMUSSEN, J. J. & STENUM, B. 1999 Shear-flow instability in a rotating fluid. *J. Fluid Mech.* **387**, 177–204.

[15] MOORE, D. W. & SAFMAN, P. G. 1969 The structure of free vertical shear layers in a rotating fluid and the motion produced by a slowly rising body. *Phil. T. R. Soc. Lond. A* **264**, 597–634.

[16] NAKABAYASHI, K. & TSUCHIDA, Y. 1995 Flow-history effect on higher modes in the spherical couette system. *J. Fluid Mech.* **295**, 43–60.

[17] NIINO, H. & MISAWA, N. 1984 An experimental and theoretical study of barotropic instability. *J. Atmos. Sci.* **41**, 1992–2011.

[18] NOIR, J., CARDIN, P., JAULT, D. & MASSON, J.-P. 2003 Experimental evidence of nonlinear resonance effects between retrograde precession and the tilt-over mode within a spheroid. *Geophys. J. Int.* **154**, 407–416.

[19] PEDLOSKY, J. 1987 *Geophysical fluid dynamics*, 2nd edn. Springer, New York.

[20] PROUDMAN, I. 1956 The almost-rigid rotation of viscous fluid between concentric spheres. *J. Fluid Mech.* **1**, 505–516.

[21] ROBERTS, P. H. & STEWARTSON, K. 1963 On the stability of a maclaurin spheroid of small viscosity. *Astrophys. J.* **137**, 777.

[22] STEWARTSON, K. 1957 On almost rigid rotations. *J. Fluid Mech.* **3**, 17–26.

[23] STEWARTSON, K. 1966 On almost rigid rotations. part 2. *J. Fluid Mech.* **26**, 131–144.

[24] YANO, J.-I. 1992 Asymptotic theory of thermal convection in rapidly rotating systems. *J. Fluid Mech.* **243**, 103–131.

[25] ZAVALA SANSON, L. & VAN HEIJST, G. J. F. 2002 Ekman effects in a rotating flow over bottom topography. *J. Fluid Mech.* **471**, 239–255.

[26] ZIKANOV, O. Y. 1996 Symmetry-breaking bifurcations in spherical couette flow. *J. Fluid Mech.* **310**, 293–324.